Available online at www.sciencedirect.com
ScienceDirect
Geochimica et Cosmochimica Acta 73 (2009) 2283–2298
Geochimica et Cosmochimica Acta
www.elsevier.com/locate/gca

Na, Mg, Ni and Cs distribution and speciation after long-term alteration of a simulated nuclear waste glass: A micro-XAS/XRF/XRD and wet chemical study

Enzo Curti [a,d,*], Rainer Dähn [a], François Farges [b,c], Marika Vespa [a,1]

[a] *Laboratory for Waste Management, Paul Scherrer Institut, CH-5232 Villigen PSI, Switzerland*
[b] *Muséum National d'Histoire Naturelle, 61 rue Buffon, 75005 Paris, France*
[c] *Department of Geological and Environmental Sciences, Stanford University, Stanford, CA 94305-2115, USA*
[d] *Helmoltz Virtual Institute "Advanced Solid-Aqueous RadioGeochemistry", Germany*

Received 10 July 2008; accepted in revised form 27 January 2009; available online 20 February 2009

Abstract

Microscopic distribution and speciation of Na, Mg, Ni and Cs in a simulated (inactive) nuclear waste glass were studied using micro X-ray fluorescence (μ-XRF) and micro X-ray absorption spectroscopy (μ-XAS), after aqueous leaching during 12 years at 90 °C. Na and Mg are major constituents of the glass that can be used to determine the progress of the glass corrosion process and the nature of secondary alteration phases. Ni and Cs represent dose determining long-lived radionuclides (^{59}Ni, ^{135}Cs) in vitrified nuclear waste.

The Na-Mg μ-XRF maps revealed that the core regions of the glass fragments are apparently unaltered and compositionally homogeneous, whereas rims and interstitial spaces are enriched with Mg-rich smectite formed during the leaching process. The micro X-ray absorption near edge structure (μ-XANES) spectra collected at the Mg K-edge in the altered zones show three sharp resonances typical for crystalline Mg-silicates. These resonances are distinctive of Mg occupying undistorted octahedral positions. In contrast, the μ-XANES spectra collected in the core zones of the glass fragments lack this resonance pattern and are identical to the spectra measured on the pristine (unleached) MW glass.

Micro extended X-ray absorption fine structure (μ-EXAFS) and μ-XANES analyses at the Ni K-edge revealed three distinct Ni(II) species: (a) Ni uniformly distributed in the glass matrix, (b) micro-inclusions with high Ni concentrations and (c) Ni associated to the Mg-clay. The comparison with reference spectra of unleached MW and other Ni-bearing silicate glasses indicated that species (a) represents the original coordinative environment of Ni in the glass. The μ-EXAFS analyses revealed that species (b) is structural Ni in trevorite ($NiFe_2O_4$), which probably formed through unmixing processes during the cooling of the glass melt. The μ-EXAFS of species (c) could be successfully modeled assuming specific adsorption or incorporation of Ni into the lattice of trioctahedral Mg-clay minerals. Alternative models assuming other elements (Ni, Al, Fe) in addition to Mg in the second shell could not be fitted successfully.

Aqueous concentration data were used to calculate the speciation of the leaching solutions. Saturation index (SI) calculations indicate undersaturation with respect to $NiCO_3$ and $NiSO_4{\cdot}7H_2O$, but oversaturation with respect to β-$Ni(OH)_2$. The latter result is probably due to the omission of Ni borate and Ni silicate complexes in the speciation calculations, for which formation constants are not available. With the help of estimation techniques, we could infer that such complexes would dominate the Ni speciation and consequently reduce the SI below the saturation of β-$Ni(OH)_2$.

* Corresponding author. Address: Laboratory for Waste Management, Paul Scherrer Institut, CH-5232 Villigen PSI, Switzerland. Fax: +41 56 310 28 21.
E-mail address: enzo.curti@psi.ch (E. Curti).
[1] Present address: Flemish organization of scientific research (FWO), Dutch-Belgian beamline, European Synchrotron Radiation Facility, 38041 Grenoble Cedex 9, France.

doi:10.1016/j.gca.2009.01.032

The μ-XRF maps show that Cs is uniformly distributed in the MW glass, since no region with high Cs concentration could be detected. The Cs L_{III}-edge μ-XAS spectra were all very similar independently of the degree of alteration, indicating similar coordination environments of Cs in the core regions of the glass as well as in the secondary clays. These spectra largely differ from that measured for pollucite (a potential secondary Cs-phase in altered glasses) implying that the coordination environments of Cs in the MW glass and in pollucite are fundamentally different.

The present study shows that μ-XRF and μ-XAS are essential tools in determining the fate and the retention mechanisms of radionuclides released from nuclear waste during aqueous alteration. Our spectroscopic analyses allowed us to exclude formation of specific Ni and Cs secondary solids (e.g. nepouite, β-$Ni(OH)_2$, pollucite) during the aqueous alteration. Ni and Cs are instead distributed as trace elements in the alteration phases formed by major elements during the leaching process. Our results imply that solid solution and/or adsorption equilibria, rather than pure phase solubility equilibria, are the adequate chemical models to determine Ni and Cs aqueous concentrations in performance assessments for radioactive waste repositories.

1. INTRODUCTION

Reprocessing and vitrification is a widely accepted option in the strategy followed by many countries to guarantee the safe disposal of nuclear high-level waste (HLW). For instance, the US, Belgium, Germany, France and Switzerland are planning to dispose vitrified waste in deep underground repositories sites hosted in appropriate geological formations (Witherspoon and Bodvarsson, 2006). Accordingly, safety analyses for such repositories must take into account glass alteration processes in risk assessment calculations. Understanding and quantifying the dissolution of vitrified nuclear waste is an essential step in such calculations, since radionuclide release from the glass will affect all subsequent steps in the prediction of radiological doses. Usually, radionuclides are assumed to be released congruently from the glass, up to elemental solubility limits defined through saturation equilibria. The limiting solids are typically simple phases, e.g. hydrous oxides, carbonates or sulfates of the specific radionuclide (Nagra, 2002).

However, most actinides and fission products, even if concentrated in the nuclear waste, are trace elements compared to major elements like Al, Si, Mg, Fe and will hardly precipitate as pure radionuclide phases. More likely, they will either co-precipitate as solid solutions with alteration phases dominated by major elements, or will be adsorbed on their surfaces. Both retention mechanisms will normally prevent aqueous concentrations from reaching the saturation of the pure radionuclide solids. As a consequence, safety assessment calculations may be over-conservative and predict exceedingly high release rates for specific radionuclides.

The investigated borosilicate glass (denoted "MW") is one of two reference formulations for reprocessed high-level radioactive waste from Swiss nuclear power plants. It corresponds to the specifications of British Nuclear Fuel Ltd. (BNFL), one of two official contractors in charge of the vitrification of Swiss high-level waste. The MW glass is a typical borosilicate glass containing about 6 wt% MgO and a number of chemical analogues (particularly lanthanides) replacing radioactive trivalent and tetravalent actinides. The second contractor (COGEMA, France) produces a glass (SON68) of similar composition but Mg-free, the Mg being replaced by an equivalent amount of Ca + Zn. A previous investigation focusing on the long-term dissolution kinetics and aqueous chemistry of both glasses showed that the glass dissolution rates of the MW glass are about ten times faster than for the SON68. This result was ascribed to the presence of Mg in the MW glass, which is supposed to accelerate the glass degradation by favoring the formation of secondary clays (Curti et al., 2006).

In the present study, we focus on the micrometer-scale mobilization and the retention mechanisms of Ni and Cs in the MW glass after alteration in pure water at 90 °C during 12 years. The nuclides ^{59}Ni and ^{135}Cs contribute significantly to the predicted overall dose in the Swiss safety assessment, partly as a result of the high solubility limits assumed in the performance assessment calculations: 3.1×10^{-5} M for Ni, based on the assumption of saturation with Ni carbonate, and unlimited solubility for Cs (Nagra, 2002). A major goal of this study was to identify the solubility-limiting secondary host phases for Ni and Cs in the altered MW glass and to shed light on their coordinative environment, both in the intact glass and in the secondary alteration products. To this aim, we used advanced X-ray techniques with high spatial resolution, notably micro X-ray diffraction (μ-XRD), micro X-ray fluorescence (μ-XRF) and micro X-ray absorption spectroscopy (μ-XAS).

In addition to Ni and Cs, spectroscopic measurements were conducted also for Mg and Na. Mg was investigated as a key major element of the glass alteration products, whereas Na served to distinguish between altered and intact glass. Such distinction was possible because Na is leached out from the glass prior to any other element through selective leaching, a process by which H_3O^+ ions diffuse into the glass and exchange for Na^+ (Vernaz and Dussossoy, 1992; Wicks et al., 1993). Therefore, sodium provided a convenient marker of the spatial extent of the corrosion process and allowed determining the penetration depth of the hydration front into the glass.

Micro-spectroscopic investigations could not be carried out on the second Swiss reference glass composition (SON68) because of the nanometric size of the secondary alteration phases (cf. Curti et al., 2006). The beam size of the X-ray microprobes used in the present investigation was too large for such small particles.

2. EXPERIMENTAL AND MODELING PROCEDURES

2.1. Sample preparation, characterization and aqueous chemistry

The MW glass was crushed and sieved to collect the fraction <160 μm. The glass powder was then washed with ethanol in an ultrasonic bath, decanted and dried at room temperature. Five 24 g aliquots of the washed powder were introduced in airtight stainless steel vessels and leached statically at 90 °C in 600 ml of distilled water. At corrosion times of 5.7 and 12.2 years, two experiments were interrupted in order to collect the leaching solution for elemental concentration analyses and the altered glass for the spectroscopic and mineralogical investigations. The wet glass was separated from the aqueous solution and stored at 100% humidity in a refrigerator ($T = 0$–10 °C). Prior to use for spectroscopic investigations, the altered glass was washed with distilled water in order to remove the interstitial solution and finally dried in the oven at 40 °C during 24 h. Due to the prolonged alteration, the glass grains and the corrosion products coalesced to form a mm-thick crust on top of the loose powder (Fig. 1). The crust was cut transversally, embedded in epoxy resin and prepared as 30 μm-thick polished thin section for optical microscopy and μ-XRF/XAS investigations. The transversal cut allowed us to study a vertical profile of the altered glass crust from top (crust–bulk solution interface) to bottom (crust- loose glass powder interface). The composition of the unleached MW glass is (in wt%): $SiO_2 = 46.7$, $B_2O_3 = 16.0$, $Na_2O = 8.5$, $Al_2O_3 = 6.6$, $MgO = 5.9$, $Li_2O = 3.9$, $REE_2O_3 = 3.4$, $Fe_2O_3 = 3.1$, $MoO_2 = 1.4$, $ZrO_2 = 1.4$, $Cs_2O = 1.1$, $Cr_2O_3 = 0.6$, $BaO = 0.5$, $NiO = 0.4$, minor oxides $= 0.5$.

Immediately after removing the vessels from the oven, an aliquot of the aqueous solution was sampled, acidified with 10 μl of concentrated HNO_3 (Merck® Suprapur) and analyzed by Atomic Emission Spectroscopy (ICP-AES) to determine the aqueous concentrations of a number of elements. For Ni and Cs, a second aliquot was centrifuged during 1 h at 95,000 *g*. The supernatant was separated and analyzed by ICP-AES together with the non-centrifuged aliquot. An additional solution sample was transferred in a glove-box flushed with N_2 for pH measurement at room temperature (23 ± 1 °C). All aqueous concentration data and pH measurements are reported in Table 1a. Errors assigned to the ICP-AES analyses correspond to instrumental uncertainties, which range from ±10% to ±30% depending on the difference between measured concentration and elemental detection limit.

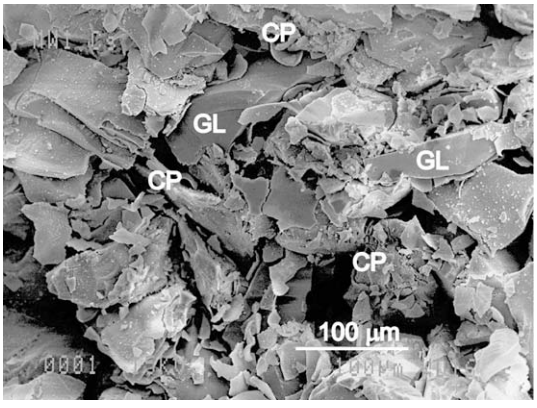

Fig. 1. SEM image of the altered MW glass, showing glass grains (GL) enveloped and cemented by flaky aggregates of corrosion products (CP), mostly clay minerals.

2.2. Aqueous speciation and saturation index calculations

Since many details of the kinetic data and wet chemical analyses collected for the MW glass were presented in an earlier publication (Curti et al., 2006), only a brief summary will be given here with focus on the results directly relevant to the spectroscopic investigations. One of the main objectives of the ICP-AES analyses was to determine, through speciation calculations, saturation indices (SI) of potential alteration phases.Table 1b and c report the calculated aqueous speciation and saturation indices of simple solids for the leaching solution collected after 12.2 years alteration time.

The speciation calculations were carried out with the MINEQL code (Westall et al., 1976), using the Nagra-PSI 01/01 thermodynamic database (Hummel et al. 2002; Thoenen and Curti, 2004) and Davies' approximation for the calculation of activity coefficients and ionic strength. Two separate Ni speciation calculations were carried out for a total Ni concentration of 1.5×10^{-7} mol/l (centrifuged sample). The first relies exclusively on the thermodynamic data selected in the Nagra-PSI 01/01 database, the second additionally includes estimated formation constants for simple Ni borate and Ni silicate complexes (see Section 4.4 for a discussion).

2.3. Data collection and reduction

The μ-XRF maps were obtained by collecting the fluorescence signal emitted from the sample within appropriate (element-specific) energy windows. Element distribution maps were generated by scanning the sample (stepwise or continuously) under a monochromatic X-ray beam. Ni-K_α and Cs-L_α maps were collected at beamline 10.3.2, Advanced Light Source (ALS), Berkeley, USA (Marcus et al., 2004) using beam sizes of about 5×5 μm. The fluorescence radiation was recorded in air using a 7-elements Ge solid state detector. Mg-K_α, Na-K_α and additional Cs-L_α μ-XRF maps were obtained at beamline LUCIA, Swiss Light Source (SLS), Villigen, Switzerland (Janousch et al., 2004; Lagarde et al., 2007) under mild vacuum and with a beam size of about 4×8 μm. The fluorescence signal was detected using a single element silicon drift diode. Sample areas of up to 1000×1500 μm were probed using X-ray energies of 1310 (Na and Mg), 5020 (Cs) and 10,000 eV (Ni).

The μ-XAS spectra at the Ni K-edge (8333 eV) and at the Cs L_{III}-edge (5012 eV) were collected for the altered glass sample and selected reference compounds on beamline 10.3.2 (ALS) using a Si(111) crystal monochromator. Moreover, μ-XANES spectra at the K-edge of Mg

Table 1
Ionic strength, pH, elemental concentrations (a), speciation (b) and saturation index calculations (c) for the MW glass leaching solution sampled after 12 years corrosion time. The saturation index (SI) is defined as the decimal logarithm of the ratio of ion activity product (IAP) to thermodynamic solubility product (K°_s) of the listed dissolution reactions. A two-term approximation (Van't Hoff equation) was applied to derive solubility products at 90 °C, using the reported reaction enthalpies.

	Elemental concentrations, ICP-AES (mol/l)				
	Measured	Detection limit		Measured	Detection limit
(a)					
Al	$(1.3 \pm 0.2) \times 10^{-4}$	2×10^{-7}	Na	$(2.1 \pm 0.3) \times 10^{-2}$	5×10^{-7}
B	$(6.5 \pm 0.7) \times 10^{-3}$	5×10^{-6}	Nd	$(7.6 \pm 0.8) \times 10^{-6}$	1×10^{-7}
Ba	$(6.3 \pm 0.6) \times 10^{-7}$	4×10^{-10}	Ni	$(2.9 \pm 0.3) \times 10^{-6}$	5×10^{-8}
Ca	$(2.2 \pm 0.3) \times 10^{-6}$	3×10^{-7}	Ni[†]	$(1.5 \pm 0.5) \times 10^{-7}$	5×10^{-8}
Ce	$(6.1 \pm 0.6) \times 10^{-6}$	4×10^{-8}	P	$(3.4 \pm 0.4) \times 10^{-5}$	2×10^{-6}
Cr	$(1.4 \pm 0.2) \times 10^{-4}$	5×10^{-8}	Pr	$(2.3 \pm 0.2) \times 10^{-6}$	1×10^{-7}
Cs	$(4.8 \pm 0.5) \times 10^{-5}$	4×10^{-7}	S	$(8.1 \pm 0.8) \times 10^{-5}$	2×10^{-6}
Cs[†]	$(3.8 \pm 0.4) \times 10^{-5}$	4×10^{-7}	Si	$(4.7 \pm 0.5) \times 10^{-3}$	9×10^{-7}
Fe	$(1.1 \pm 0.1) \times 10^{-5}$	2×10^{-7}	Sm	$(9.3 \pm 1.0) \times 10^{-7}$	1×10^{-7}
K	$(4.1 \pm 0.4) \times 10^{-4}$	2×10^{-7}	Sr	$(1.4 \pm 0.2) \times 10^{-6}$	6×10^{-10}
La	$(2.6 \pm 0.3) \times 10^{-5}$	1×10^{-8}	Th	<Detection limit	1×10^{-7}
Li	$(2.9 \pm 0.3) \times 10^{-2}$	1×10^{-6}	U	<Detection limit	1×10^{-7}
Mg	$(9.0 \pm 0.9) \times 10^{-5}$	3×10^{-8}	Y	$(1.1 \pm 0.1) \times 10^{-6}$	3×10^{-9}
Mn	$(2.6 \pm 0.3) \times 10^{-7}$	5×10^{-9}	Zn	$(1.1 \pm 0.1) \times 10^{-7}$	4×10^{-8}
Mo	$(6.9 \pm 0.7) \times 10^{-4}$	1×10^{-5}	Zr	$(6.9 \pm 0.7) \times 10^{-6}$	6×10^{-8}

pH and ionic strength (I)			Inorganic carbon[*]		
I	0.053	mol/l	C(tot)	1.0×10^{-5}	mol/l
pH (90 °C)	9.1	Calculated	pCO_2	6.7×10^{-7}	atm
pH (23 °C)	9.6	Measured	CO_3^{2-}	1.5×10^{-6}	mol/l

Major species (mmol/l)				Ni species (mol/l)		
				Ni species	No Ni-B/Si complexes	With Ni-B/Si complexes
(b)						
Li^+	29.0	$Si(OH)_4$,aq	1.9	Ni^{+2}	1.5×10^{-8}	5.5×10^{-10}
Na^+	20.6	$SiO(OH)_3^-$	2.7	$NiPO_4^-$	2.0×10^{-8}	7.2×10^{-10}
K^+	0.4	OH^-	0.8	$NiOH^+$	1.1×10^{-7}	4.1×10^{-9}
$B(OH)_3$,aq	19.7	MoO_4^{2-}	0.7	$NiBO(OH)_2^+$	—	1.0×10^{-7}
$B(OH)_4^-$	45.3	HPO_4^{2-}	0.02	$NiSiO(OH)_3^+$	—	4.4×10^{-8}

Reaction data and SI calculations[a]

Reaction	$\log K^{\circ}_s$ (25 °C)	$\Delta_r H^{\circ}_m$ (kJ/mol)	$\log K^{\circ}_s$ (90 °C)	log IAP (90 °C)	SI (90 °C)
(c)					
β-$Ni(OH)_2(cr) + 2H^+ = Ni^{2+} + 2H_2O$	10.5	*−59.934*	8.62[b]	9.85	1.2
				8.41[c]	−0.2[c]
$NiCO_3(cr) = Ni^{2+} + CO_3^{2-}$	*−11.2*	*63.930*	*−9.20*	−14.45	−5.3
				−15.88[c]	−6.7[c]
$NiSO_4{\cdot}7H_2O(cr) = Ni^{2+} + SO_4^{2-} + 7H_2O$	*−2.267*	*12.167*	*−1.89*	−12.83	−10.9
				−13.88[c]	−12.0[c]
$BaCO_3(cr) + H^+ = Ba^{2+} + HCO_3^-$	1.767	−11.961	1.39	−2.94	−4.3
$BaSO_4(cr) = Ba^{2+} + SO_4^{2-}$	−9.97	26.575	−9.14	−11.12	−2.0
$SrCO_3(cr) + H^+ = Sr^{2+} + HCO_3^-$	1.058	−16.576	0.54	−2.58	−3.1
$SrSO_4(cr) = Sr^{2+} + SO_4^{2-}$	−6.632	−4.339	−6.77	−10.75	−4.0
$Mg(OH)_2(cr) + 2H^+ = Mg^{2+} + 2H_2O$	16.84	−113.386	13.28	13.19	−0.1
$MgCO_3(cr) + H^+ = Mg^{2+} + HCO_3^-$	2.041	−45.819	0.60	−1.28	−1.9
$MnCO_3(cr) + H^+ = Mn^{2+} + HCO_3^-$	−0.801	−20.884	−1.46	−3.68	−2.2
$FeCO_3(cr) + H^+ = Fe^{2+} + HCO_3^-$	−0.561	−25.278	−1.35	−2.74	−1.4
$FeSO_4{\cdot}7H_2O(cr) = Fe^{2+} + SO_4^{2-} + 7H_2O$	−2.209	20.536	−1.57	−10.91	−9.3
$Al(OH)_3(cr) + 3H^+ = Al^{3+} + 3H_2O$	7.756	−102.784	4.53	4.27	−0.3
$Al_2Si_2O_5(OH)_4(cr) + 6H^+ = 2Al^{3+} + 2Si(OH)_4 + H_2O$	7.435	−147.7	2.80	3.11	0.3
$MoO_3(cr) + H_2O = MoO_4^{2-} + 2H^+$	−12.055	33.02	−11.02	−21.66	−10.6
$SiO_2(cr) + 2H_2O(l) = Si(OH)_4$,aq	−3.746	20.647	−3.10	−2.72	0.4
$SiO_2(am) + 2H_2O(l) = Si(OH)_4$,aq	−2.714	14.594	−2.26	−2.72	−0.5
$ZrO_2(cr) + 4H^+ = Zr^{4+} + 2H_2O$	−1.9	10.845	−1.56	1.68	3.2

[*] Calculated assuming initial water equilibrated with air and subsequent closure of the vessel.
[†] Supernatant after centrifugation.
[a] Thermodynamic data from Hummel et al. (2002) except italicized values (from Gamsjäger et al., 2005).
[b] Value consistent with $\log K^{\circ}_s$ (90 °C) = 8.4 ± 0.3 derived from the experimental data of Gamsjäger et al. (2002).
[c] log IAP and SI values calculated assuming formation of Ni silicate and borate complexes.

(1303.0 eV) and additional μ-XAS spectra at the Cs L_{III}-edge were recorded on the same glass sample and on selected reference compounds at the LUCIA beamline, using pairs of beryl crystals (for Mg and Na K-edge measurements) and Si(1 1 1) crystals (for the Cs L_{III}-edge measurements). All μ-XAS spectra were collected in fluorescence mode.

Reduction and modelling of the μ-XAS data was performed with the ATHENA/ARTEMIS package (Ravel and Newville, 2005). The statistical parameters used to evaluate the goodness of the EXAFS fits were the multiple correlation coefficient (*R*-factor) and the reduced χ^2 (chi-square) as calculated by ARTEMIS. The *R*-factor measures the misfit between modeled and experimental Fourier transformed (FT) spectra, whereas χ^2 expresses the same misfit scaled to the estimated data uncertainty and to the number of free fit parameters (for rigorous definitions, see Bevington, 1969; Downward et al., 2007).

Energy conversion to wave vector units ($Å^{-1}$) was carried out by assigning the origin (E_0) to the first inflection point of the absorption edge. The monochromator angle at the 10.3.2 beamline was calibrated using a Ni metal foil ($E_0 = 8333$ eV). At LUCIA, energy calibration for the beryl crystals was made by matching a NaCl (halite) reference spectrum measured during the beam time to the data of Neuville et al. (2004) ($E_{peak\_b} = 1076.5$ eV). For the Si(1 1 1) crystals, the K-edge inflection point of metallic Ag ($E_0 = 3351$ eV), which was brought on the sample in the form of tiny orientation marks, was used. Fitting and modelling of the Ni-K EXAFS spectra were carried out with FEFF 8.20 (Rehr et al., 1991) using the XRD structures of talc (Gruner, 1934) and trevorite (Subramanyam, 1971) as starting models. Radial structure functions (RSF) of the Ni K-edge μ-EXAFS spectra were obtained by Fourier transformation (FT) of the k^3-weighted $\chi(k)$ functions over the range of 1.9-12.4 $Å^{-1}$ (location A2) and 1.9-11.2 $Å^{-1}$ (location T2) using a Kaiser–Bessel window and a smoothing parameter of four. Multishell fit analyses were carried out in the range of 1.0–3.5 Å (preliminary model) and of 1.0–5.0 Å (refined model) for location A2. A range of 1.0–6.0 Å was set for the spectrum measured at location T2.

At the Cs L_{III}-edge, attempts to model the EXAFS spectra were unsuccessful due to the interference with the Ba L_{III}-edge at $E - E_0 \sim 230$ eV, which limited the usable *k*-range for the FT to 7 $Å^{-1}$. For the Mg spectra, a μ-XANES analysis was carried out through comparison with adequate reference spectra. EXAFS was not possible due to the interference of the Al K-edge at 1560 eV.

Mineralogical investigations included X-ray diffraction measurements with conventional powder diffraction and with a focused synchrotron beam, as well as scattering and transmission electron microscopy (SEM, TEM). The micro-analytical data obtained from the TEM measurements and the conventional powder diffraction data are described in detail elsewhere (Curti et al., 2006). Micro X-ray diffraction measurements were performed in transmission mode on dry, altered MW glass powders at beamline 10.3.2 (ALS) using a 14 keV beam of 5 × 5 μm size and a Bruker CCD camera to detect the diffracted beam. Experimental parameters, such as sample-detector distance and detector plane orientation, were refined using the diffraction image of α-Al_2O_3 reference powder. The two-dimensional diffraction images were then converted to 1-dimensional lattice plane distance (*d*) vs. intensity diagrams using the FIT2D package (Hammersley, 1995).

3. RESULTS

3.1. Aqueous chemistry

The calculated aqueous speciation (Table 1b) is complex due to the large number of elements present in the glass. The leaching solutions are dominated by species of the soluble elements B, Li and Na, which also determine the ionic strength. The pH remained remarkably constant (9.6 ± 0.2 at 23 °C) during the entire duration of the experiment, owing to the buffering capacity of the boric acid/borate system ($pK_a = 9.2$). In the first Ni speciation calculation, based exclusively on selected thermodynamic data (i.e. neglecting the possible formation of Ni borate/silicate complexes), $NiPO_4^-$, Ni^{2+} and particularly $NiOH^+$ are the major Ni species, whereas in the second calculation Ni borate and Ni silicate complexes dominate.

Saturation indices were calculated using solubility products and reaction enthalpies from Gamsjäger et al. (2005) and Hummel et al. (2002) for a number of simple solids (Table 1c), including β-$Ni(OH)_2$(cr), $NiCO_3$(cr) and $NiSO_4·7H_2O$(cr). Other potentially relevant Ni solids were not considered because either the solubility products were unreliable or the available thermodynamic data insufficient for an extrapolation to 90 °C. Our *SI* calculations indicate strong undersaturation with respect to Mo(VI) oxide and all considered sulfate and carbonate minerals, including $NiCO_3$(cr) and $NiSO_4·7H_2O$(cr). Strong oversaturation was found with respect to β-$Ni(OH)_2$ and crystalline ZrO_2, whereas the remaining minerals are all close to saturation ($-0.3 \leqslant SI \leqslant 0.4$). These results will be further commented later (Sections 4.4 and 4.5).

It is important to realize that the computed saturation indices critically depend on the thermodynamic data used for the prevailing Ni complexes, as these directly affect the activity of the free Ni^{2+} ion ($a_{Ni^{2+}}$).The formation constant and reaction enthalpy used for $NiOH^+$, $\log K^\circ_s$ (25 °C) = −9.5 and $\Delta_r H^\circ_m = 51.8$ kJ mol^{-1}, can be considered to be reliable as they practically coincide with the values selected in a recent comprehensive review of Ni thermodynamic data published by the Nuclear Energy Agency (NEA) (Gamsjäger et al., 2005). In contrast, the thermodynamic data used to calculate the concentrations of Ni borate and silicate complexes have high uncertainties, since they were derived through empirical estimation techniques (Section 4.4).

Another important issue is related to the fact that most SI were computed using ICP-AES data obtained from non-centrifuged solutions. Thus, except for Cs and Ni, we cannot rule out the possibility that the determined aqueous concentrations are biased by the presence of colloids. Consequently, in cases where $SI > 0$ is calculated, solutions might in reality be undersaturated with respect to the solid

of interest. The presence of colloids in the leaching solution was indeed detected (compare Ni and Cs concentrations of non-centrifuged and centrifuged solutions in Table 1A). On the other hand, whenever undersaturation is calculated using concentration data of non-centrifuged solutions (as for the large majority of the tested solids), the results are valid *a fortiori* because the real dissolved element concentration would be even less than indicated by the ICP-AES measurements.

3.2. μ-XRD investigations

Conventional X-ray diffraction measurements on the altered MW glass powder obtained in a previous study (Curti et al., 2006) yielded reflections matching the powder diffraction patterns of saponite, hectorite and montmorillonite, indicating that the major corrosion product of the altered MW glass is a smectite.

Other Mg-rich clay minerals can be excluded based on the interlayer spacing. The obtained value of 13.2 Å is typical for smectites with a single layer of interlayer water (Meunier, 2005), whereas palygorsite, sepiolite and vermiculite have well defined, either smaller or larger interlayer spacings (10.4 ± 0.1, 12.2 ± 0.2 and 14.2 ± 0.2 Å, respectively). Moreover, these minerals generate additional important reflections that are not detected in the powder diffraction pattern of the MW glass sample.

In the present study, μ-XRD data at lower *d*-spacings ($d = \sim 1.4$–2.2 Å) were obtained with a microfocused 14 keV beam, revealing a number of additional reflections. Although most of them could be attributed to montmorillonite, at least two prominent reflections cannot be assigned to smectite minerals (Fig. 2). Our analysis revealed that the three most intense reflections match the major lines in the magnetite–trevorite series ($Fe^{II}Fe^{III}{}_2O_4$–$Ni^{II}Fe^{III}{}_2O_4$). Thus, these results indicate the presence of a Ni-rich spinel phase in the investigated MW glass sample.

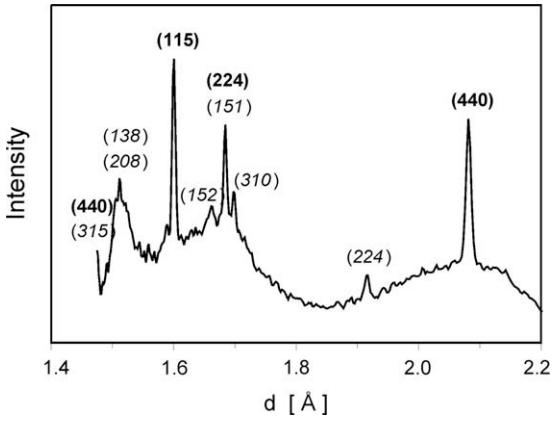

Fig. 2. Raw μ-XRD pattern obtained from the magnetic fraction of the altered MW glass powder, compared with the indexed reflections of trevorite (bold) and montmorillonite (normal typeface, italicised). Only the most intense reflections contributing to a given peak have been indexed for montmorillonite.

3.3. μ-XRF investigations

Selected μ-XRF elemental distribution maps of the MW glass sample are shown in Fig. 3. Fig. 3a is a two-color map showing Na (red) and Mg (green) distributions. The map reveals the granular structure of the glass powder and provides insights into the nature of the alteration process. The orange-colored areas represent glass regions with uniform Na and Mg concentration, whereas the green-colored areas at the periphery of the glass fragments and partially filling the interstitial space are Mg-rich, but Na-depleted. The dark areas are domains of low mineral density. Since Na is rapidly leached out during the aqueous alteration of silicate glasses via alkali-proton exchange (Wicks et al., 1993), the interface between orange and green areas marks the reaction front of the glass corrosion reaction. Thus, the orange areas represent pristine glass apparently unaffected by the corrosion process, whereas the green-colored areas represent altered regions. In a previous TEM study (Curti et al., 2006), the altered zone was found to consist dominantly of Mg-rich smectites that envelope and partly cement the glass grains (see also Fig. 1).

Fig. 3b and c are μ-XRF elemental distribution maps of Ni and Cs, respectively, over the areas corresponding to the inserts shown in Fig. 3a. Whereas the Cs distribution within the glass grains appears to be fairly uniform (the variations in intensity are smooth and can be ascribed to thickness or illumination effects), the Ni map reveals the presence of tiny "hot spots" (10 μm max.) with high Ni concentration (e.g. white spot at location T2).

The μ-XRF maps thus provide the structural–morphological information necessary for selecting appropriate locations for the μ-XAS investigations, owing to the heterogeneity of the sample. For instance, they make it possible to select spots within regions of apparently unaltered glass and within Mg-rich corrosion products. In many cases, μ-XAS spectra of Mg, Ni and Cs could be collected at exactly the same location, allowing inter-elemental correlations.

3.4. μ-XANES investigations at the Mg K-edge

In Fig. 4a, normalized Mg K-edge μ-XANES spectra from the altered MW glass are compared with experimental spectra of reference compounds, including a spectrum collected on a pristine, unleached sample of the MW glass (top spectrum denoted *ugl*). The probed spots, shown on the μ-XRF maps of Fig. 3, can be divided into two distinct groups: Those labelled C1, C2,... ("set 1") were measured in the apparently unaltered core regions of the glass fragments (the orange-colored regions in Fig. 3), whereas the spectra labelled A1, A2,... ("set 2") were collected in the peripheral zones rich in alteration products (the green-colored regions in Fig. 3, mainly Mg-clay particles). Fig. 4a readily shows distinctive features in the Mg K-edge μ-XANES spectra from the two mentioned domains. The spectra at locations C1 and C2 ("set 1") are fairly smooth and show little structure, whereas the "set 2" spectra (A1, A2, A3) are characterized by three sharp resonances within the main absorption peak (labelled A–C), followed by two additional weak oscillations (D and E). Spectrum C3 has

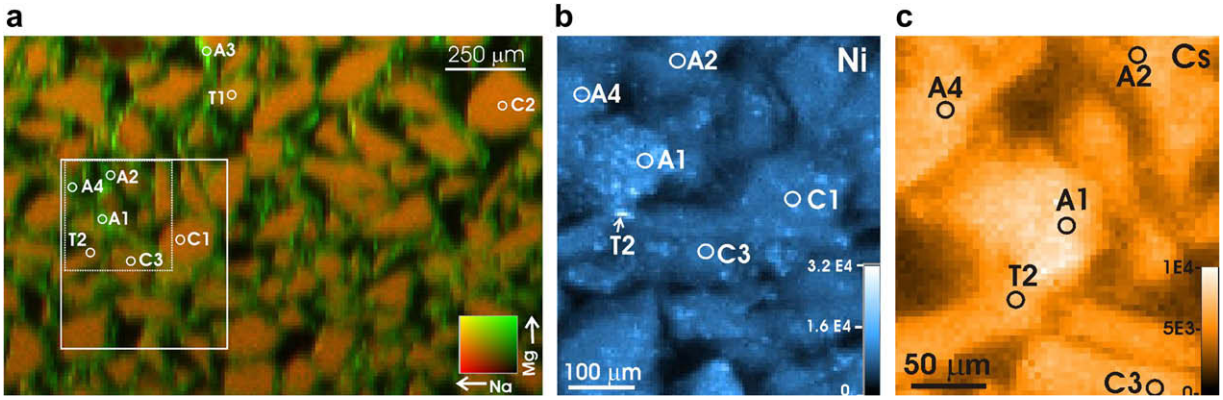

Fig. 3. (a) Bicolor map of the combined Na-K_α and Mg-K_α fluorescence signals with locations and labeling of spots probed with µ-XAS measurements. The color coding given in the insert RG map represents relative Na and Mg concentrations in the sample. (b) Ni elemental distribution map corresponding to the insert area (solid line) shown in Fig. 3a. (c) Cs elemental distribution map corresponding to the insert area (dotted line) shown in Fig. 3a. The color scale bars indicate I_0-normalized count rates.

features intermediate between the two sets of data, suggesting that a mixture of unaltered glass and corrosion products was probed at that location.

A further look at Fig. 4a shows that the spectra collected in the altered region ("set 2") are strikingly similar to those of diopside, glaucophane, talc and of the clay minerals lizardite and montmorillonite. Following spectral features characterize the "set 2" spectra: (a) the resonant energies are invariant, although the relative intensities of peaks A and C vary in the different probed spots (cf. spectra A2 and A3); (b) the energies of peaks A–D closely match those of lizardite; (c) peak E is at an energy 1–2 eV higher than for lizardite and matches exactly the corresponding peak in diopside.

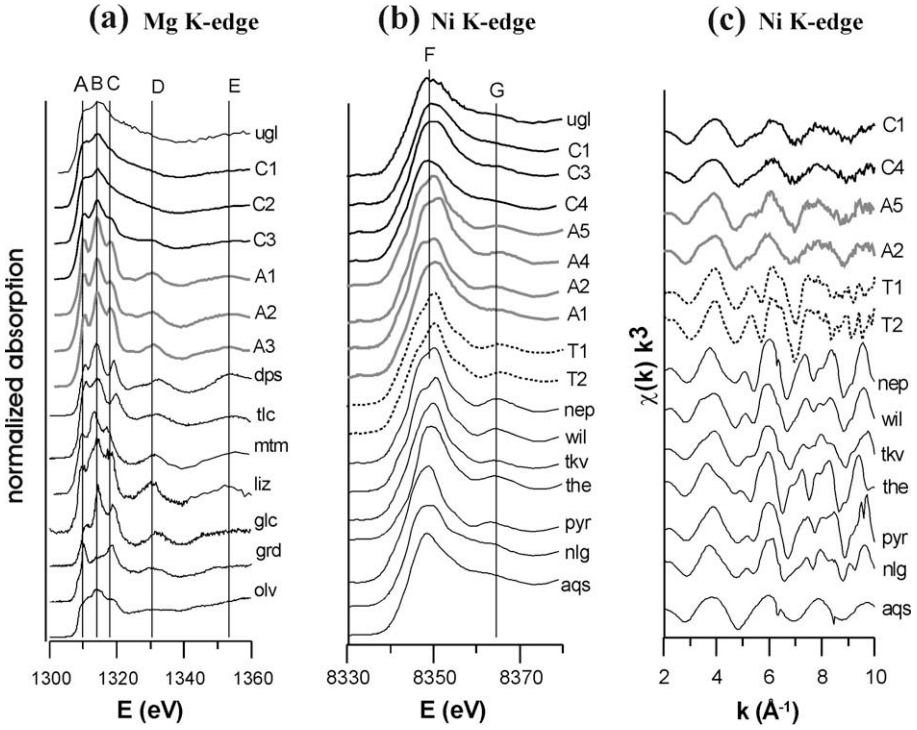

Fig. 4. Mg K-edge µ-XANES (a), Ni K-edge µ-XANES (b) and Ni K-edge µ-EXAFS spectra (c). The spectra are labeled as follows: ugl = pristine, unleached MW glass, A1–A5 = altered regions of leached MW glass, C1–C4 = apparently unaltered regions of leached MW glass, T1–T2 = Ni-rich micro-inclusions in leached MW glass. Mineral references: dps = diopside; tlc, talc; mtm, montmorillonite; liz, lizardite; glc, glaucophane; grd, grandidierite; olv, olivine; nep, nepouite; wil, willemseite; tkv, takovite; the, theophrastite; pyr, pyrope; nlg, nullaginite; aqs, $Ni(NO_3)_2$ aqueous solution.

3.5. μ-XANES investigations at the Ni K-edge

Several μ-XANES and μ-EXAFS spectra were collected at the Ni K-edge from the altered MW glass sample (Fig. 4b and c). Some of them were obtained at the same locations (cf. Fig. 3a and b) of the previously described Mg K-edge spectra, thus enabling cross-correlations between Ni and Mg μ-XANES data. In Fig. 4b, Ni K-edge μ-XANES spectra from the altered MW glass can be compared with the spectra of the unleached MW glass (*ugl*) and of several Ni reference compounds. As for Mg, the Ni K-edge spectra obtained in the alteration zone and in regions apparently unaffected by the alteration have distinctive features. For instance, most absorption spectra from the altered zone (locations A2, A4, A5) have spectral features ($F = 8347.2$ eV, $G = 8364.5$ eV) which are absent, or weaker, in the spectra recorded at the centre of glass grains (locations C1 and C3). Among the reference compounds, inflection F (occurring just before the white line peak) appears only in the spectra of the Ni-clay minerals nepouite and willemseite (Ni-talc), whereas it is absent in all other reference spectra. Therefore, in analogy to the Mg μ-XANES, the Ni μ-XANES spectra collected within the altered glass show features consistent with the spectra of clay minerals, which do not appear in the spectra collected in the core regions of the glass fragments (locations C1, C3, C4).

For location A1, however, the analogy fails: Although the Mg K-edge μ-XANES spectrum at location A1 closely resembles those collected at other locations rich in interstitial corrosion products, the corresponding Ni K-edge μ-XANES bears more resemblances to those collected in the unaltered core zone of glass fragments. This inconsistency may be a consequence of the largely different volumes probed at the Mg K- and Ni K-edges, resulting from the different penetration depths of the X-rays in the corresponding energy regions (1.3 keV at the Mg-K-edge, 8.3 keV at the Ni K-edge). Possibly, the Ni K-edge μ-XANES spectrum collected at location A1 (with a beam penetrating the entire sample thickness of 30 μm) might be dominated by spectral contributions originating from the unaltered glass buried below the surface of the thin section, whereas the corresponding Mg K-edge μ-XANES spectrum shows only contributions originating from the alteration products present in the first 2–3 μm below the sample surface. A comparison of Fig. 3a and b seems to confirm this interpretation: In the Mg map (Fig. 3a) location A1 appears to lie in an Mg-rich interstitial zone, whereas the same spot appears to be embedded in the core region of a glass grain in the Ni and Cs maps. Differences in the volumes probed by soft and hard X-rays are unavoidable and should always be considered when absorption spectra or XRF maps of different elements are correlated.

In analogy to Mg, the Ni μ-XANES spectra from the core regions of the glass fragments are very similar to the spectrum recorded for the unleached glass (*ugl*). This is a clear indication that the internal zones of the glass fragments remained unaffected by the aqueous corrosion process.

Fig. 4c shows selected k^3-weighted $\chi(k)$ functions of the Ni K-edge μ-EXAFS spectra, most of them corresponding to the μ-XANES spectra in Fig. 4b. It reveals two new aspects, which will be discussed in Sections 4.2 and 4.3: (a) the spectra recorded for the high-Ni inclusions (T1 and T2) have oscillation patterns fundamentally different from all other MW-glass spectra, thus indicating the presence of a third Ni species in the altered MW sample; (b) none of the Ni reference spectra shown in Fig. 4c has oscillation patterns matching any of the spectra collected from the altered MW glass sample.

3.6. Ni μ-EXAFS investigations

Detailed Ni K-edge μ-EXAFS analyses were carried out for the spectra collected at location T2, a Ni-rich hot spot, and location A2, which lies in the interstitial zone rich in secondary Mg-clays. Based on the previously discussed μ-XRD data, we attempted to fit the T2 μ-EXAFS spectrum using trevorite as model structure (Subramanyam, 1971). The results of our best fit, shown in Table 2 and Fig. 5, indicate a good agreement between the FT experimental spectrum and the EXAFS model. The distances determined for the four nearest backscattering pairs (Ni–O, Ni–Ni_1, Ni–Fe_1, Ni–Ni_2) coincide within the experimental uncertainties with those from the XRD structural data of trevorite. The low coordination numbers obtained for the Ni–Ni_1 and Ni–Fe_1 shells ($CN_{Ni-Ni1} = 3.9 \pm 0.3$ instead of 6, $CN_{Ni-Fe1} = 4.3 \pm 0.7$ instead of 6) may be explained by experimental artefacts, (e.g. overabsorption), by structural disorder, or by a cation defective structure. Non-stoichiometric spinels are common and may form through partial oxidation of magnetite (Fe_3O_4) to the isomorphous maghemite (Fe_2O_3) (Lagoeiro, 1998).

The μ-EXAFS analysis carried out for the spectrum collected at location A2 is summarized in Table 3 and Fig. 6. A three shell fit including Ni–O, Ni–Mg and Ni–Si backscattering pairs (Fig. 6a and b) was performed using talc as a starting structural model (Gruner, 1934) and assuming that a single central Ni^{2+} absorber replaces an octahedrally coordinated Mg^{2+} ion. Thus, this model simulates the backscattering from an isolated Ni absorber (trace element) in an Mg-rich silicate matrix (Ni–Ni pairs were not included in this fit).

Our best fit yields Ni–O, Ni–Mg and Ni–Si distances within the typical ranges of Mg-phyllosilicates. The fitted coordination numbers for the Ni–O and Ni–Si shells are also close to the ideal values for octahedral sites in phyllosilicates, whereas the coordination number obtained for the Ni–Mg backscattering pairs is only half the theoretical value of six. Fixing CN_{Ni-Mg} to six always yielded unacceptably large uncertainties or unrealistic fit parameters. We also tested a refined model with additional shells around the Ni absorber over the range $R + \Delta R = 1.2$–5.0 Å. In this model, the coordination numbers were fixed to values characteristic for trioctahedral clays, except for CN_{Ni-Mg}, which was set to three as in the previous 3-shell fit. We obtained in this way a more accurate fit of the experimental *k*-space and FT spectra, with reasonable Debye–Waller factors and interatomic distances close to the values determined with XRD methods for talc (Fig. 6c and d and Table 3b). The following alternative structural models with Ni, Fe or Al

Table 2
Results of the μ-EXAFS fit for the Ni-K-edge spectrum obtained at location T2. Fixed parameters are given in italics.

	N	(ΔN)	R (Å)	(ΔR)	σ^2 (Å^2)
Ni–O	5.3 ± 0.4	(−0.7)	2.03 ± 0.01	(−0.01)	*0.005*
Ni–Ni_1	3.9 ± 0.3	(−2.1)	2.92 ± 0.01	(−0.03)	*0.005*
Ni–Fe_1	4.3 ± 0.7	(−1.7)	3.47 ± 0.02	(+0.01)	*0.007*
Ni–Ni_2	*12*		5.07 ± 0.03	(−0.04)	0.011 ± 0.002
Ni–Fe_2	*8*		5.63 ± 0.14	(+0.21)	0.021 ± 0.019
Ni–Fe_3	*12*		6.07 ± 0.14	(+0.17)	0.011 ± 0.004

$\Delta E_0 = 2.8 \pm 1.4$ eV; $S_0 = 0.85$; R-factor = 0.041, reduced $\chi^2 = 23.61$.
N, coordination number; R, interatomic distance; σ^2, Debye–Waller factors; ΔE_0, energy shift; S_0, amplitude reduction factor.
ΔN, ΔR deviation from N, R in the XRD model structure of trevorite (Subramanyam, 1971).

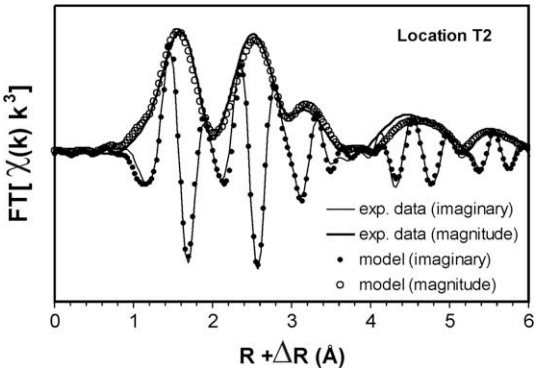

Fig. 5. Fit of the Fourier transformed (FT) Ni K-edge μ-EXAFS spectrum collected at location T2, using the structure of trevorite as starting model.

backscatterers in the second shell were tested: (a) Ni–O, Ni–Al, Ni–Si, (b) Ni–O, Ni–(Mg + Ni), Ni–Si, (c) Ni–O, Ni–(Mg + Al), Ni–Si, (d) Ni–O, Ni–(Mg + Fe), Ni–Si. All these models yielded poor fits (either unacceptable parameter values or exceedingly high uncertainties) and must therefore be discarded. We conclude that the μ-EXAFS spectrum collected at location A2 can be reasonably fitted only assuming Ni–O, Ni-Mg and Ni-Si pairs.

3.7. Principal component analysis and linear combination fits

Due to the small particle size in the MW sample, collecting spectra resulting from the superposition of different Ni species was unavoidable. Therefore, a principal component analysis (PCA) was carried out in order to determine number and identity of the spectral components required to reproduce each single experimental absorption spectrum. Based on the results of the PCA analysis, linear combinations fits (LCF) were then calculated to determine the relative contributions of the identified spectral components to each single experimental spectrum. Our procedure closely follows the technique described in detail by Manceau et al. (2002), implemented in the programs available from beamline 10.3.2 at ALS. For the LCF calculations the in-built utility in ATHENA was used.

Table 3
Results of μ-EXAFS fits for the Ni K-edge spectrum obtained for location A2. Fixed parameters are given in italics. (a) 3-shell fit; (b) refined 8-shell fit with fixed coordination numbers.

	N	N phs.*	R (Å)	R phs.*	σ^2 (Å^2)
(a)					
Ni–O	5.3 ± 0.3	6	2.05 ± 0.01	2.05–2.09	*0.006*
Ni–Mg	3.1 ± 1.6	6	3.08 ± 0.03	3.03–3.07	*0.008*
Ni–Si	4.5 ± 1.6	4	3.26 ± 0.02	3.16–3.26	*0.008*
	N	N talc*	R (Å)	R talc*	σ^2 (Å^2)
(b)					
Ni–O	*6*	6	2.05 ± 0.01	2.06	$0.007 \pm .0005$
Ni–Mg	*3*	6	3.08 ± 0.05	3.03–3.04	0.008 ± 0.004
Ni–Si	*4*	4	3.25 ± 0.05	3.16–3.18	0.008 ± 0.004
Ni–O	*2*	2	3.52 ± 0.13	3.38	0.007 ± 0.017
Ni–O	*4*	4	3.80 ± 0.08	3.67	0.010 ± 0.007
Ni–O	*4*	4	4.03 ± 0.04	4.00	0.004 ± 0.004
Ni–Si	*4*	4	4.42 ± 0.05	4.38–4.42	0.010 ± 0.006
Ni–O	*16*	16	4.54 ± 0.18	4.53–4.76	0.042 ± 0.043

$\Delta E_0 = 2.8 \pm 1.7$ eV; $S_0 = 0.85$; R-factor = 0.020; reduced $\chi^2 = 6.26$.
$\Delta E_0 = 2.6 \pm 2.1$ eV; $S_0 = 0.85$; R-factor = 0.018, reduced $\chi^2 = 5.37$.
N, coordination number; R, interatomic distance; σ^2, Debye–Waller factors; ΔE_0, energy shift; S_0, amplitude reduction factor.
* Interatomic distances and coordination numbers for Mg in phyllosilicates (phs.) and talc structures, compiled from the ICSD database (Bergerhoff and Brown, 1987).

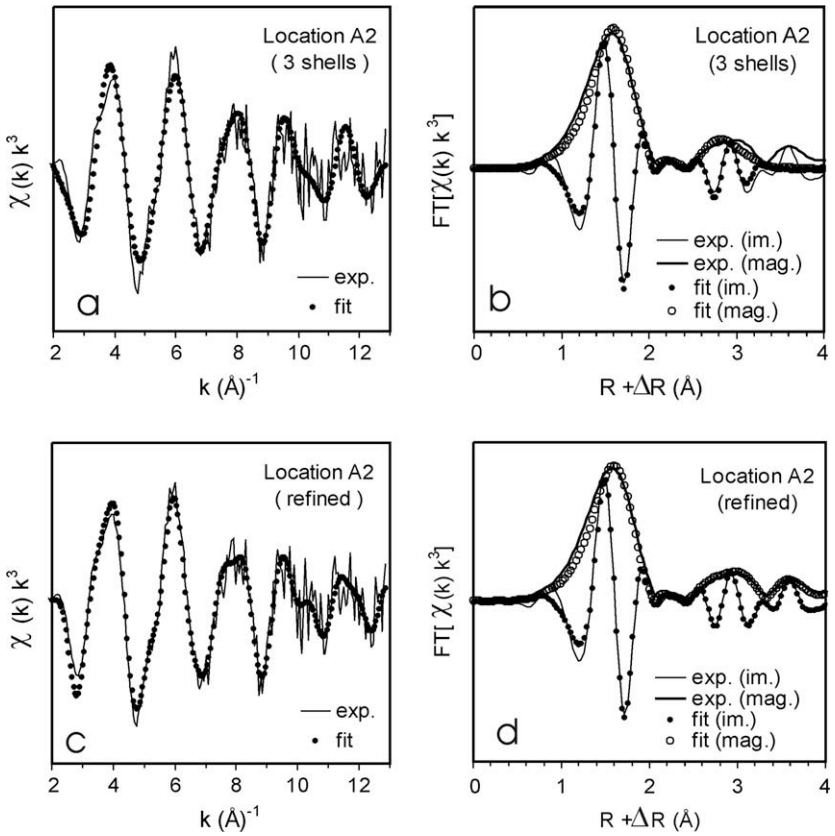

Fig. 6. Fits of the Fourier transformed (FT) Ni K-edge μ-EXAFS spectra collected at location A2, using the talc structure as starting model. Left: k^3 weighted normalized spectra; right: magnitude and imaginary part of FT, uncorrected for phase shift: (a and b) 3-shell fit, (c and d) refined 8-shell fit.

The previously discussed μ-EXAFS analysis showed that at least three distinct Ni species occur in the altered MW glass, exemplified by the spectra collected at location A2 (Ni associated to secondary Mg-phyllosilicates), location C1 (Ni associated to the pristine glass) and location T2 (trevorite inclusion). The PCA analysis confirmed that three components are necessary and sufficient to describe all experimental spectra, as the minimum of the "indicator function" lies between 3 and 4 components. The "indicator function" is related to the eigenvalues of the matrix used to decompose the experimental spectra in a given number of components, and reaches a minimum for the appropriate number of "abstract" components to use. The next step was to replace the "abstract" components with real candidate "end-member" spectra and to compute for each of them the "spoil function" after carrying out a "target transformation" (Manceau et al., 2002). The "spoil function" tests the likelihood that a given reference spectrum represents a true component in a series of unknown multicomponent spectra: the lower its value, the more likely is the selected candidate "end-member" spectrum. Manceau et al. (2002) give an upper acceptance limit of 4.5 for a candidate spectrum. As potential "end-members" we tested the spectra of Ni reference compounds as well as the MW experimental spectra collected at locations A2, C1 and T2, which appeared as the most distinctive among all spectra measured in the altered MW glass. The results (Table 4) show that the three MW spectra at locations A2, C1 and T2 are indeed appropriate to carry out LCF calculations. The spectrum of β-$Ni(OH)_2$ also yields a good score but can be eliminated since the presence of a Ni hydroxide phase can be ruled out (Ni–Ni pairs could be excluded in the EXAFS analysis and the XRF maps did not reveal the presence of concentrated Ni phases in the altered zone). Ni-pyrope, which also has an acceptable score, can be ruled out as it cannot form at ambient conditions (stability in the high p, T range).

Based on the results of the PCA analysis, we carried out LCF calculations on a number of spectra collected in the altered MW glass sample. The results, presented in Table 5, show that the spectra can be interpreted as mixtures of the three selected "end-member" spectra identified in the MW glass. In most cases two components are sufficient to fit the experimental spectra, but in a few cases all three components are required.

3.8. Cs μ-XAS investigations

Cs L_{III}-edge μ-XAS spectra were measured for pollucite ($Na_{0.3}Cs_{0.7}[H_2O]_{0.3}AlSi_2O_6$), a secondary Cs-phase found in altered simulated nuclear waste glasses (Ribet and Gin, 2004; Inagaki et al., 2006), and on representa-

Table 4
"Spoil function" values of nine postulated "end-member" spectra (including the three MW glass spectra C1, T2 and A1 showing the most distinctive features) tested on the 11 experimental XAS spectra listed in Table 5. The "end-member" spectra selected for subsequent LCF calculations are shown in bold.

Assumed "end-member"	Spoil function
Location C1 (pristine glass)	**2.1**
Location T2 (trevorite inclusion)	**2.2**
β-$Ni(OH)_2$	2.4
Location A2 (secondary Mg-clay)	**3.4**
Ni-pyrope	4.2
Nullaginite	5.5
Widgiemoolthalite	5.6
Nepouite	9.9
Ni^{2+}(aq)	13.8

tive locations of the altered MW glass sample. All the k^3-weighted $\chi(k)$ μ-XAS spectra collected from the altered MW glass proved to be strikingly similar. No significant difference could be stated between spectra collected in altered and non-altered glass domains, suggesting similar Cs coordinative environments in both glass regions. Fig. 7 shows representative spectra from the core zones of glass fragments (locations C3, C5), from the Mg-rich altered zone (locations A1, A2, A5 and A6), as well as the reference spectrum of a natural pollucite. Since the latter has a different oscillation pattern, the coordinative environment of Cs in the MW glass and in pollucite must be fundamentally different. Based on the large number of Cs μ-XAS spectra collected from the leached MW glass, and the lack of Cs-rich spots in the extensive μ-XRF maps collected, we conclude that there was no precipitation of secondary pollucite or any other Cs solid during the aqueous alteration of the glass.

Due to the interference of the Ba-L_{III} absorption edge and the presence of the $[2p_{3/2}4_p]$ multi-electron excitation at 5.0 $Å^{-1}$ (Arčon et al., 2005) the usable k-range for the Cs L_{III}-edge spectra collected on the MW glass was too limited for a meaningful EXAFS analysis.

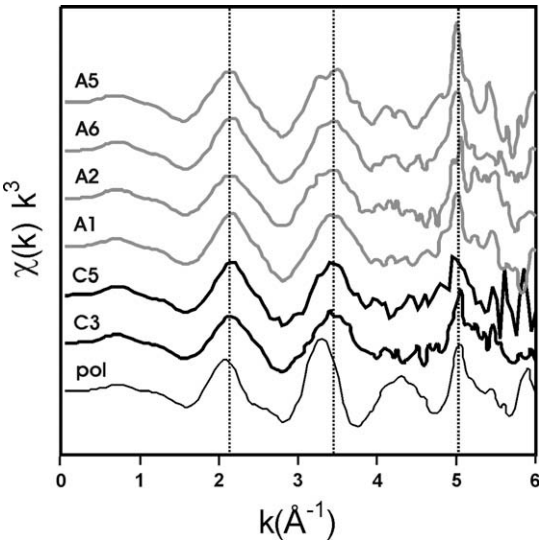

Fig. 7. Representative Cs L_{III}-edge μ-XAS spectra from leached MW glass (C3, C5 = core regions of glass grains; A1–A6 = altered Mg-rich regions) compared to the experimental spectrum of pollucite (pol). The sharp peak at a 5 $Å^{-1}$ is due to a multi-electron excitation.

4. DISCUSSION

4.1. μ-XRF maps

The Ni, Na, Mg and Cs μ-XRF maps yielded essential insights in the alteration process of the simulated nuclear waste glass MW. They show that, upon prolonged aqueous dissolution at mildly alkaline pH, important fractions of Cs and Ni—representing the long-lived radionuclides ^{135}Cs and ^{59}Ni—co-precipitate almost *in situ* with Mg-rich secondary alteration products. Both Ni and Cs appear to be uniformly distributed in the alteration products. Micro-domains with high Ni or Cs concentration are absent in the altered zone, indicating that no specific Ni or Cs phase (e.g. Ni–hydroxide, nepouite or pollucite) precipitated during the aqueous leaching process. The latter result is further strengthened by the μ-XAS data collected on the MW glass,

Table 5
Results of LCF calculations for Ni-K spectra collected from the altered MW glass assuming the spectra of locations A2, C1 and T2 as "end-member" components.

Spectrum ID	Zone*	Statistics			% Spectral component		
		R	χ^2	χ^0	A2	C1	T2
MWK1b-8	Core	9.8E-05	1.8E-02	1.1E-04	0	100	0
MWK1-7	Core	4.6E-05	7.8E-03	5.0E-05	14	86	0
MWK1-A	Core	4.6E-05	8.0E-03	5.1E-05	0	96	4
MWK1-11	cp	4.2E-05	7.4E-03	4.8E-05	66	0	34
MWK1b-9	cp	7.7E-05	1.4E-02	8.6E-05	64	22	14
MWK1-12	cp	2.0E-05	3.4E-03	2.2E-05	24	46	30
MWK1-D	cp	2.1E-05	3.7E-03	2.4E-05	69	19	13
MWK1-G	cp	5.5E-05	1.0E-02	6.5E-05	85	0	15
MWK1-8	cp, Mg hs	3.8E-05	6.5E-03	4.2E-05	63	4	33
MWK1-9	cp, Mg hs	2.4E-05	4.1E-03	2.6E-05	38	0	62
MWK1-6	cp, Ni hs	2.4E-05	4.0E-03	2.6E-05	18	0	82

* Core, centre of glass grain; cp, corrosion product; hs, high concentration (hot spot) $R = \Sigma(\chi_{data} - \chi_{fit})^2/\Sigma(\chi_{data})^2$.

which allowed us to exclude Ni–Ni pairs in the Ni-K μ-EXAFS analysis and failed to reveal oscillation patterns matching the spectrum of pollucite, the only secondary Cs-phase detected so far in altered nuclear waste glasses.

4.2. Mg and Ni K-edge μ-XANES

The Mg-K-edge μ-XANES spectra collected in the altered domains of the MW glass show a triple resonance pattern typical of Mg-silicates (e.g. diopside, montmorillonite, lizardite, talc, glaucophane), which is lacking in the core zones of the glass fragments.

Some clues to the interpretation of these results are provided by the work of Cabaret et al. (1998), who measured Mg K-edge absorption spectra for two Mg-pyroxenes (diopside and enstatite) and compared them with theoretical full multiple-scattering (FMS) calculations. They deduced that the resonances A, C and D (Fig. 4a) are related to medium order multiple-scattering effects, since these features disappeared when the radius of the modeled atomic cluster around the central Mg absorber was reduced to less than 6 Å. In order to interpret their Mg K-edge XANES spectra, Li et al. (1999) followed an empirical approach based on the cross-comparison of a large number of spectra of Mg-minerals, all well characterized in terms of crystal structure. They selected compounds with Mg–O coordination numbers of IV (spinel), V (grandidierite), V + VI (yoderite), VI (forsterite and several chain and sheet silicates) and VIII (pyrope). A deconvolution analysis allowed these authors to determine that the position of peak A shifts to lower energies with decreasing coordination number of the first Mg–O shell. These shifts are significant only for Mg coordination changes from VIII to VI/V, or from VI/V to IV. A clear distinction between V-fold coordinated and VI-fold coordinated Mg can be made on the base of peak B, which almost disappears in the V-fold coordinated compound grandidierite (Fig. 4a). The comparison of the MW glass spectra A1, A2, A3 with those of the mentioned reference compounds indicates that Mg has VI-fold coordination in the secondary phase formed during the MW glass alteration. In addition, the correspondence of the A–D peak positions to the lizardite spectrum indicates that the main corrosion product is a clay mineral with trioctahedral (brucite-type) sheet structure. This result is consistent with XRD and TEM data, which indicate that the main alteration product is an Mg–smectite (Curti et al., 2006).

On the other hand, the strong similarity between the Mg-K spectrum obtained from the pristine unaltered glass (*ugl*) and the C1 and C2 spectra collected from the cores of glass fragments in the altered MW sample leaves no doubt that Mg occurs there in its original coordination environment, whereas for the C3 spectrum a component originating from alteration products is evident. The C3 spectrum was collected on a severely altered, small-sized glass grain, so that the chance of including spectral contributions from the secondary clay was higher than for spots C1 and C2.

In analogy to the Mg-XANES results, also the Ni μ-XANES spectra collected in the core regions of the glass fragments (locations C1, C3, C4) show smooth oscillation patterns indicative of the low-order environment peculiar to vitreous materials. This interpretation is confirmed by the similarity between the Ni K-edge spectra collected from the core regions of the MW glass fragments and the spectrum of the unleached MW glass (Fig. 4b), as well as of other Ni-bearing reference glasses (Farges et al., 2001a,b). Among the four glasses selected for the comparison (Fig. 8a), the glass ALB 0.004 has the spectrum and chemical composition most closely resembling to those of unaltered domains in the MW glass. According to the empirical correlation set up in Farges et al. (2001a), the energy position of the Ni-K pre-edge peak in the unaltered MW glass (8331.0 ± 0.2 eV, see Fig. 8b) is also characteristic of a pristine vitreous environment, indicating either V-fold coordinated or a mixture of IV and VI-fold coordinated Ni–O sites.

In conclusion, the Mg K-edge and Ni K-edge μ-XANES spectra (Fig. 4a and b) are found to correlate well with the degree of glass alteration. Whereas the Mg-K and Ni-K spectra from the core zones of the MW glass fragments have features characteristic of pristine, unleached silica glasses, those collected in the altered zones display patterns (particularly the resonance triplet in the Mg K-edge and inflection F in the Ni K-edge) consistent with Mg and Ni coexistence in an Mg-dominated, crystalline silicate. This phase has been identified by XRD and TEM investigations as a smectite with composition midway between hectorite and montmorillonite (Curti et al., 2006), whereas other low-temperature Mg-clay phases (palygorsite, talc, serpentine, vermiculite, sepiolite) could be ruled out based on incompatible XRD patterns.

4.3. Ni K-edge μ-EXAFS

The Ni K-edge μ-EXAFS spectra collected in the clay-rich regions of the altered MW glass could be successfully modelled assuming Ni as isolated absorber surrounded by Mg and Si atoms. The fits yielded interatomic distances consistent with the crystal structure of smectites, thus confirming the XRD findings.

The low coordination number (about three) determined for the Ni–Mg pairs may be explained by assuming Ni adsorption on the edge sites of the clay. In their P-EXAFS study, Dähn et al. (2003) found configurations with N(Ni–Al) ~ 2 and N(Ni–Si) ~ 4 for Ni adsorbed on montmorillonite edge sites, with distances similar to those obtained for Ni–Mg and Ni–Si pairs in our fit of the spectrum obtained at location A2. In a trioctahedral Mg-clay, analogous structural positions would yield N(Ni–Mg) = 3 and N(Ni–Si) = 4, as in our EXAFS analysis. Accordingly, the coordination environment of Ni atoms associated to the Mg-rich clay in the altered MW glass would be analogous to that of species Ni_3 in Dähn et al. (2003) (see Fig. 12 in mentioned reference).

On the other hand, the low Ni–Mg coordination number may also be a consequence of structural disorder, experimental bias (e.g. overabsorption, see Heald, 1988), or incorporation of Li^+ (a light element with a very low backscattering power) in a hectorite structure (Ianovici

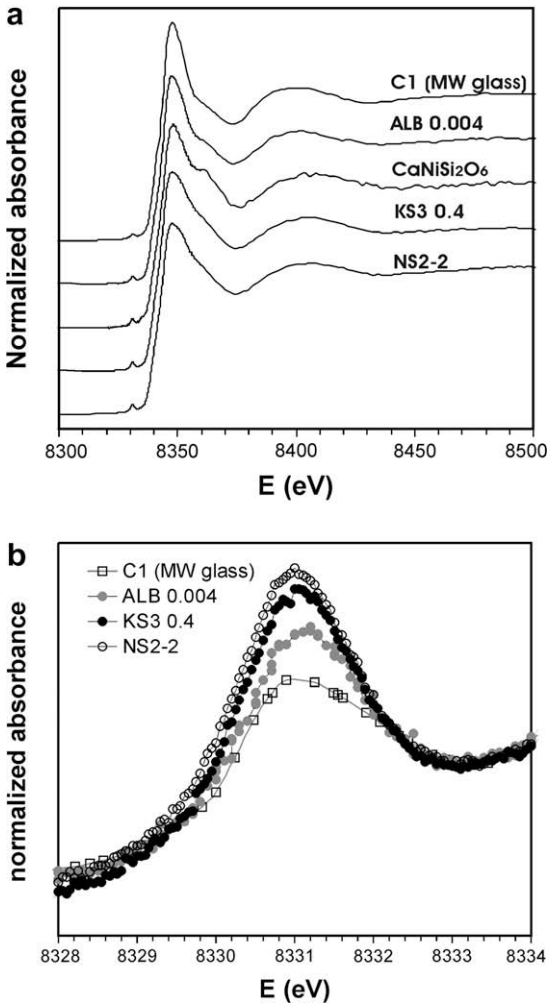

Fig. 8. Comparison of C1 spectrum (MW glass, non-altered domain) with Ni K-edge spectra of unleached Ni-bearing glasses (from Farges et al., 2001a): (a) XANES spectra, (b) pre-edge.

et al., 1990). Therefore, lattice incorporation cannot be excluded as the main Ni retention mechanism in the MW secondary clay. This interpretation seems even more appropriate, since all fitted distances and all other coordination numbers agree with a lattice incorporation model. In the case of surface adsorption, Ni–Si coordination numbers of about two are expected (cf. Table 2 in Dähn et al., 2003), whereas our fit yields a coordination number of about four.

The μ-XRF maps also revealed the presence of Ni-rich "hot spots" embedded in a homogeneous glass matrix with uniform Ni concentration, which were identified through μ-EXAFS analyses and μ-XRD measurements as trevorite ($NiFe_2O_4$) micro-inclusions. Such inclusions are not the product of low-temperature aqueous alteration, but primary heterogeneities that form in Ni-bearing glasses during cooling of the glass melt (Lutze, 1988). Therefore, two distinct primary Ni species (Ni uniformly distributed in the glass matrix and trevorite inclusions) are present in the unleached MW glass. Such bimodal distribution in the pristine glass suggests that two distinct release mechanisms may operate during the release of ^{59}Ni from vitrified nuclear waste.

4.4. Ni and Cs solubility

The aqueous concentration data obtained from the leaching solutions were used to calculate the chemical speciation of dissolved Ni and saturation indices for potential secondary phases. For these calculations, we used only the critically reviewed thermodynamic data reported by Hummel et al. (2002) and Gamsjäger et al. (2005). As discussed by Hummel and Curti (2003) other data should not be used due to severe internal inconsistencies. In the case of Cs, the available thermodynamic data were insufficient to carry out such calculations with an acceptable degree of confidence, and even for Ni this task proved to be difficult.

As noted previously, the results of our μ-XRF/XAS investigation failed to reveal the occurrence of concentrated Ni phases in the secondary products formed during the aqueous alteration of the MW glass. This observation is in principle consistent with our analysis of the aqueous solution data, since the calculated saturation indices for Ni carbonate, hydrous Ni sulfate (both strongly undersaturated) and β-$Ni(OH)_2$ (oversaturated) are all far from equilibrium (SI = 0). However, the latter result is surprising, as it implies that the solution is metastable with respect to crystalline nickel hydroxide even after an ageing time of 12 years at the relatively high temperature of 90 °C. Although more soluble forms of $Ni(OH)_2$ exist with solubility products up to 2.5 log units higher than for the crystalline form (Feitknecht and Schindler, 1963) one would expect formation of β-$Ni(OH)_2$ under such conditions, as demonstrated in the solubility study carried out by Gamsjäger et al. (2002) in the 30–80 °C temperature range.

A possible explanation for the calculated oversaturation is that potentially important Ni-borate and Ni-silicate complexes, for which no thermodynamic data are available in the literature, had forcedly to be neglected in the speciation calculations. The scarce data available on borate complexes of other transition metals like Cu, Cd and Zn (van den Berg, 1984), indicate that such complexes do indeed exist and cannot be ignored at such high B and Si concentrations. In order to assess the potential role of Ni-borate and Ni-silicate complexes on the solubility of Ni hydroxide, we estimated the formation constants at 25 °C for the $NiBO(OH)_2^+$ and $NiSiO(OH)_3^+$ complexes by applying the correlation method of Schwarzenbach (1961). This estimation technique is based on the premise that H^+ can be regarded as a hard metal. Therefore, for any other metal, there should be a correlation between the stability constants of its complexes and the strength of the corresponding acids. For instance, $NiCl^+$ is expected to be weaker than $NiCO_3(aq)$ because HCl dissociates much more easily ($pK_a << 0$) than HCO_3^- ($pK_a = 6.4$). By plotting the known Ni-ligand formation constants against the corresponding acid dissociation constants leads to a crude correlation, from which unknown formation constants of Ni with other ligands can be roughly extrapolated. Because $B(OH)_3$ and $Si(OH)_4$ are weak acids ($pK_a = 9.3$. and 9.9,

respectively) large formation constants are expected for the complexes $NiBO(OH)_2^+$ and $NiSiO(OH)_3^+$.

Such a correlation plot was constructed using the data compiled in Gamsjäger et al. (2005), yielding $\log \beta^o_1 = 3.5 \pm 1.0$ for $NiBO(OH)_2^+$ and $\log \beta^o_1 = 3.6 \pm 1.0$ for $NiSiO(OH)_3^+$ (Fig. 9). Introducing these constants in our chemical speciation model led to a Ni speciation dominated by the Ni-borate and Ni-silicate complexes (summing up to >95% of the total dissolved Ni) and a decrease of the Ni^{2+} activity by orders of magnitude. As a consequence the *SI* for β-$Ni(OH)_2$ was reduced to a value below saturation (−0.2, see Table 1).

Due to its large cationic size and low charge, Cs^+ is not expected to form strong complexes with any of the major ligands present in the glass leaching solution. The thermodynamic database used in our calculations does not list any Cs complex or solid, resulting in 100% of the measured Cs-concentration as free Cs^+ ion and no precipitation reaction. The ICP-AES analyses yielded Cs concentrations of $(4.8 \pm 1.9) \times 10^{-5}$ M before centrifugation and $(3.8 \pm 1.5) \times 10^{-5}$ M after centrifugation. Using the latter concentration and the glass dissolution rates reported in Curti et al. (2006) we calculated that about 95% of the Cs released from the glass is retained in the alteration products. This figure is even higher for Ni (>96%). Such results demonstrate that the dissolution process was highly incongruent for both radionuclides. As a consequence, only a minor fraction of the Cs and Ni inventories released through glass dissolution is mobile.

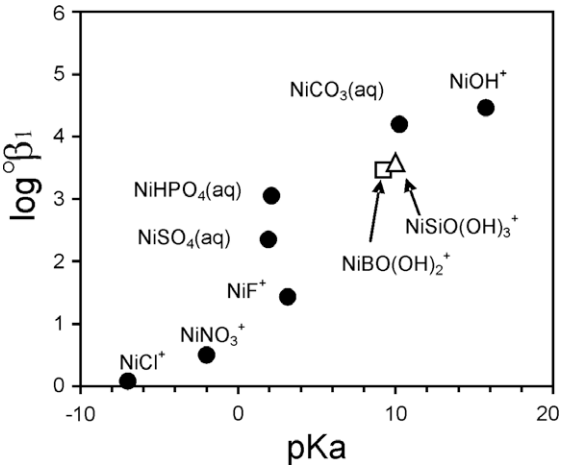

Fig. 9. Estimation of formation constants for the hypothetical complexes $NiBO(OH)_2^+$ and $NiSiO(OH)_3^+$ through correlation of known Ni formation constants with the corresponding acid dissociation constants (pK_a-values). The known formation constants (solid circles) were taken from Gamsjäger et al. (2005), whereas pK_a-values are from Lide (2007). The unknown constants (at 25 °C) were extrapolated linearly from the mono-sulfate and mono-hydroxo constants, yielding $\log \beta^o_1 \sim 3.5 \pm 1.0$ for $NiBO(OH)_2^+$ and $\log \beta^o_1 \sim 3.6 \pm 1.0$ for $NiSiO(OH)_3^+$. The pK_a of water was converted for consistency with the reference state definition of the other constants: $pK_w^* = pK_w + \log(55.56 \text{ mol/kg } H_2O) = 14 + 1.74 = 15.74$ (this is necessary because in pK_w the activity of water is defined in terms of mole fraction). The pK_a values for HCl (−7) and HNO_3 (−2) are not known exactly and are only rough approximations.

Our results show that calculating the solubility of Cs and Ni in the glass leaching environment is not a trivial task and requires robust thermochemical data for all relevant chemical species (including the solid phases). Despite the key role of boron during the dissolution of nuclear waste glasses, this issue has been largely ignored to date, making theoretical calculations of metal solubility in such environments an arduous task. Presently, we are not in a position to model precisely Ni and Cs aqueous concentrations in the complex nuclear waste glass system. Nevertheless, our data show that even radionuclides like ^{135}Cs, assumed to be entirely soluble in safety assessment (Nagra, 2002) are efficiently retained in secondary alteration products during the corrosion of nuclear glasses. Such beneficial effects are currently neglected in repository performance calculations.

4.5. Saturation index calculations

In addition to the previously discussed Ni phases, saturation indices were calculated also for a number of other simple solids that could precipitate in the investigated chemical system (Table 1C). All carbonates and sulfates, as well as the crystalline Mo(VI) oxide, are strongly undersaturated, so that precipitation of these solids in their pure form can be safely ruled out. In contrast, the calculated *SI*-values of brucite, gibbsite and kaolinite are close to saturation, implying that precipitation of these minerals during the alteration of the MW glass cannot be excluded.

In the case of SiO_2, the activity of $Si(OH)_4$ ($10^{-2.72}$) is midway between quartz and amorphous silica saturation. Such activities are typical of equilibrium with micro-crystalline quartz (e.g. chalcedony). An indication for the presence of micro-crystalline quartz in the alteration products of the MW glass is indeed provided by the powder-XRD data, which show a weak broad peak centred at $d = 3.35$ Å (see Fig. 10 in Curti et al., 2006). In contrast, the XRD data yielded no evidence for the presence of brucite, gibbsite or kaolinite.

Finally, it is noted that the strong oversaturation with respect to crystalline Zr oxide (baddeleyite) is possibly an indication that the leaching solution is in equilibrium with an amorphous form of Zr oxy-hydroxide. Experimental data show that amorphous, colloidal $Zr(OH)_4$ readily precipitates when a base is added to Zr-bearing solutions, yielding equilibrium concentrations several orders of magnitude higher than for crystalline ZrO_2 (see Appendix D in Brown et al., 2005).

5. CONCLUSIONS

In this paper, we present the results of X-ray spectroscopic investigations carried out at micrometric resolution on a simulated nuclear waste glass (MW) that was subject to aqueous alteration at 90 °C during more than 12 years. Our results show that the alteration of such glasses is a geochemically complex process involving dissolution and partial *in situ* re-precipitation of Ni and Cs radionuclides. Detailed μ-XAS/XRF analyses in combination with other

techniques (XRD, μ-XRD, TEM) allowed us to determine that an important fraction of the dissolved Ni is immobilized as trace element in trioctahedral Mg-rich smectites precipitated during the aqueous alteration of the MW glass. As for Ni, a substantial part of the Cs released from the glass was also found to be trapped as trace element in the alteration products. However, the local atomic coordination environment of Cs could not be determined due to the limited *k*-range available for the EXAFS analysis. In both cases, no specific concentrated (Ni or Cs) phase was formed during the glass alteration process.

The speciation model of the leaching solution indicated unexpectedly oversaturation with respect to β-$Ni(OH)_2$. In conjunction with the X-ray spectroscopic data, which show that no secondary Ni solid phase precipitated, this result would suggest metastability of the solution, which however is unlikely after a leaching time of 12 years at 90 °C. We could argue that this apparent inconsistency is probably a consequence of the use of an incomplete thermodynamic dataset in the speciation calculation, since potentially important Ni borate and silicate complexes—for which formation constants are unavailable—could not be taken into account. With the help of estimation techniques, it could be shown that such complexes would dominate the aqueous speciation of Ni in the aqueous phase and drastically reduce the calculated SI.

Our results also imply that pure phase saturation equilibria are not always adequate tools for predicting aqueous radionuclide concentrations in safety assessments for nuclear waste repositories. This study suggests that solubility limits for Cs and Ni in the pore water permeating the nuclear waste glass should be determined based on adsorption and/or solid solution equilibria. Unfortunately, this task is currently not feasible due to the lack of adequate thermodynamic data.

Finally, our study evidences once more the important role of clay minerals, notably smectites, as alteration products of silicate glasses. As shown by Crovisier et al. (1992) crystalline smectites formed as major secondary phase of Icelandic basalts altered by ice melting water. A recent study on the corrosion of historical Roman glasses (1800 a) also shows the formation of Mg-smectite as major alteration product (Verney-Carron et al., 2008). Since in both cases the alteration proceeded over millennia, smectite must be considered as a stable end-product of the aqueous leaching of Mg-bearing silica glasses.

ACKNOWLEDGMENTS

We thank the ALS (Advanced Light Source, Lawrence Livermore National Laboratory at Berkeley, USA) and SLS (Swiss Light Source, Paul Scherrer Institut, Villigen, Switzerland) for providing the high-quality beamtime and infrastructure necessary for our synchrotron-based investigations. The ALS is supported by the Director, Office of Science, Office of Basic Energy Sciences, Materials Sciences Division of the US Department of Energy under Contract DE-AC03-76SF00098 at the Lawrence Berkeley National Laboratory. The authors gratefully acknowledge beamline scientists M. Marcus (10.3.2, ALS) and M. Janousch (LUCIA, SLS) for their invaluable support during data acquisition. Dominik Kunz (Paul Scherrer Institut, Laboratory for Waste Management) is warmly thanked for his help during the acquisition of μ-XAS/XRF experimental data. Partial financial support was provided by the National Cooperative for the Disposal of Radioactive Waste (Nagra), Wettingen, Switzerland.

REFERENCES

Arčon I., Kodre A., Padežnik Gomilšek J., Hribar M. and Mihelič A. (2005) Cs L-edge EXAFS atomic absorption background. *Phys. Scripta* **T115**, 235–236.

Bergerhoff G. and Brown I. D. (1987) In Crystallographic Databases (eds. F. H. Allen, G. Bergerhoff and R. Sievers), International Union of Crystallography, Chester, pp. 77–95.

Bevington Ph. R. (1969) *Data Reduction and Error Analysis for the Physical Sciences*. McGraw-Hill, New York, 336 p.

Brown P. L., Curti E. and Grambow B. (2005) In Chemical Thermodynamics of Zirconium. Chemical Thermodynamics (eds. F. J. Mompean, J. Perrone and M. Illemassène). Nuclear Energy Agency (NEA), vol. 8. Organisation for Economic Co-operation and Development (OECD), 512p. ISBN 0-444-52125-9.

Cabaret D., Sainctavit Ph., Ildefonse Ph. and Flank A. M. (1998) Full multiple scattering calculations of the X-ray absorption near edge structure at the magnesium K-edge in pyroxene. *Am. Mineral.* **83**, 300–304.

Crovisier J. L., Honnorez J., Fritz B. and Petit J. C. (1992) Dissolution of sub glacial volcanic glasses from Iceland: laboratory study and modeling. *Appl. Geochem. Suppl. Iss.* **1**, 55–81.

Curti E., Crovisier J. L., Karpoff A. M. and Morvan G. (2006) Long-term corrosion of two nuclear waste reference glasses (MW and SON68): a kinetic and mineral alteration study. *Appl. Geochem.* **21**, 1152–1168.

Dähn R., Scheidegger A. M., Manceau A., Schlegel M., Baeyens B., Bradbury M. H. and Chateigner D. (2003) Structural evidence for the sorption of Ni(II) atoms on the edges of montmorillonite clay minerals: a polarized X-ray absorption fine structure study. *Geochim. Cosmochim. Acta* **67**(1), 1–15.

Downward L., Booth C. H., Lukens W. W. and Bridges F. (2007) A variation of the *F*-test for determining statistical relevance for particular parameters in EXAFS analysis. In *X-Ray Absorption Fine Structure XAFS13: 13th International Conference, July 9–13, 2006*. AIP Conference Proceedings **882**, 129 (2007), LBNL-62566.

Farges F., Brown, Jr., J. E., Petit P. E. and Munoz M. (2001a) Transition elements in water-bearing silicate glasses/melts. Part I: a high-resolution and anharmonic analysis of Ni coordination environments in crystals, glasses, and melts. *Geochim. Cosmochim. Acta* **65**(10), 1665–1678.

Farges F., Munoz M., Siewert R., Malavergne V., Brown, Jr., G. E., Behrens H., Nowak M. and Petit P. E. (2001b) Transition elements in water-bearing silicate glasses/melts. Part II: Ni in water-bearing glasses. *Geochim. Cosmochim. Acta* **65**(10), 1679–1693.

Feitknecht W. and Schindler P. (1963) Solubility constants of metal oxides, metal hydroxides and metal hydroxide salts in aqueous solution. *Pure Appl. Chem.* **1**(2), 130–199.

Gamsjäger H., Wallner H. and Preis W. (2002) Solid-solute phase equilibria in aqueous solutions XVII. Solubility and thermodynamic data of nickel(II) hydroxide. *Monatsh. Chem. (Chemical Monthly)*. **133**, 225–229.

Gamsjäger H., Bugajski, J., Gaida, T., Lemire, R. and Preis W. (2005) In *Chemical Thermodynamics of Nickel. Chemical Thermodynamics* (eds. F. J. Mompean and M. Illemassène). Nuclear Energy Agency (NEA), vol. 6. Organisation for Economic Co-operation and Development (OECD), 617p. ISBN 0-444-51802-9.

Gruner J. W. (1934) The crystal structures of talc and pyrophyllite. *Z. Kristallogr. Krist.* **88**, 412–419.

Hammersley A. P. (1995) FIT2D Reference Manual. *ESRF Internal Report, EXP/AH/95-01*. European Synchrotron Research Facility, Grenoble, France.

Heald S. M. (1988) Design of an EXAFS experiment. In *X-Ray Absorption: Principles, Applications, Techniques of exafs, sexafs and xanes*, (eds. D. C. Koningsberger and R. Prins), vol. 92. Chemical Analysis, Wiley, New York, pp. 87–118.

Hummel W., Berner U., Curti E., Pearson, Jr., F. J. and Thoenen T. (2002) Nagra/PSI Chemical Thermodynamic Data Base 01/01. Nagra Technical Report NTB 02-16, Nagra, Wettingen, Switzerland and Universal Publishers/uPublish.com, Parkland, Florida, 565p. ISBN 1-58112-620-4.

Hummel W. and Curti E. (2003) Nickel aqueous speciation and solubility at ambient conditions: a thermodynamic elegy. *Monatsh. Chem. (Chemical Monthly)* **134**, 941–973.

Ianovici V., Neacşu G. and Neacşu V. (1990) Li-bearing stevensite from Moldova Noua, Romania. *Clays Clay Miner.* **38**(2), 171–178.

Inagaki Y., Shinkai A., Idemistu K., Arima T., Yoshikawa H. and Yui M. (2006) Aqueous alteration of Japanese simulated waste glass P0798: effects of alteration-phase formation on alteration rate and cesium retention. *J. Nucl. Mater.* **354**, 171–184.

Janousch M., Flank A.-M., Lagarde P., Cauchon G., Bac S., Dubuisson J. M., Schmidt T., Wetter R., Grolimund D. and Scheidegger A. M. (2004) LUCIA—a new1–7 keV μ-XAS beamline. *AIP Conf. Proc.* **705**, 312–315.

Lagarde P., Flank A. M., Vantelon D. and Janousch M. (2007) Micro-soft X-ray spectroscopy with the LUCIA beamline. *AIP Conf. Proc.* **882**, 852–857.

Lagoeiro L. E. (1998) Transformation of magnetite to hematite and its influence on the dissolution of iron oxide minerals. *J. Metamorph. Geol.* **16**, 415–423.

Li D., Peng M. and Murata T. (1999) Coordination and local structure of magnesium silicate minerals and glasses: Mg K-edge XANES study. *Can. Mineral.* **37**, 199–206.

Lide D. R. (2007) *CRC Handbook of Chemistry and Physics*. 88th ed., 2640p. ISBN-10:0849304881.

Lutze W. (1988) Silicate glasses. In *Radioactive Waste Forms for the Future* (eds. W. Lutze and R. C. Ewing). Amsterdam, North-Holland, pp. 1–159.

Manceau A., Matthew A. M. and Tamura N. (2002) Quantitative speciation of heavy metals in soils and sediments by synchrotron X-ray techniques. In *Applications of Synchrotron Radiation in Low-Temperature Geochemistry and Environmental Science* (eds. P. Fenter, M. Rivers, N. Sturchio and S. Sutton), Reviews in Mineralogy and Geochemistry, vol. 49, Mineralogical Society of America, pp. 341–428.

Marcus M. A., MacDowell A. A., Celestre R., Manceau A., Miller T., Padmore H. A. and Sublett R. E. (2004) Beamline 10.3.2 at ALS: a hard X-ray microprobe for environmental and materials sciences. *J. Synchrotron Radiat.* **11**, 239–247.

Meunier A. (2005) *Clays*. Springer Verlag, 472p. ISBN 3-540-21667-7.

Nagra (2002) *Project Opalinus Clay—Safety Report, Nagra*, Technical Report NTB 02-05, Nagra, Wettingen, Switzerland.

Neuville D. R., Cormier L., Flank A. M., Prado R. J. and Lagarde P. (2004) Na-K edge XANES spectra of minerals and glasses. *Eur. J. Mineral.* **16**, 809–816.

Ravel B. and Newville M. (2005) ATHENA, ARTEMIS, HEPHAESTUS: data analysis for X-ray absorption spectroscopy using IFEFFIT. *J. Synchrotron Radiat.* **12**, 537–541.

Rehr J. J., Mustre de Leon J., Zabinsky S. I. and Albers R. C. (1991) Theoretical X-ray absorption fine structure standards. *J. Am. Chem. Soc.* **113**, 5135–5140.

Ribet S. and Gin S. (2004) Role of neoformed phases on the mechanisms controlling the resumption of SON68 glass alteration in alkaline media. *J. Nucl. Mater.* **324**, 152–164.

Schwarzenbach G. (1961) The general, selective and specific formation of complexes by metallic cations. In *Advances in Inorganic Chemistry and Radiochemistry* (eds. Emeléus H. J. and Sharpe A. G.), vol. 3. Academic Press, New York, pp. 275–285.

Subramanyam K. N. (1971) Neutron and X-ray diffraction studies of certain doped nickel ferrites. *J. Phys. C* **4**, 2266–2268.

Thoenen T., Berner U., Curti E., Hummel W. and Pearson F.J. Jr. (2004). Development and application of the Nagra/PSI chemical thermodynamic database 01/01. In *Energy, Waste and the Environment: a Geochemical Perspective* (eds. R. Giere and P. Stille), vol. 236. Geological Society Special Publications, London, pp. 561–577.

van den Berg C. M. G. (1984) Speciation of boron with Cu^{2+}, Zn^{2+}, Cd^{2+} and Pb^{2+} in 0.7 M KNO_3 and in sea-water. *Geochim. Cosmochim. Acta* **48**(12), 2613–2617.

Vernaz E. Y. and Dussossoy J. L. (1992) Current state of knowledge of nuclear waste glass corrosion mechanisms: the case of R7T7 glass, *Appl. Geochem.* Suppl. Issue No. **1**, 13–22.

Verney-Carron A., Gin S. and Libourel G. (2008) A fractured roman glass block altered for 1800 years in seawater: analogy with nuclear waste glass in a deep geological repository. *Geochim. Cosmochim. Acta* **72**(22), 5372–5385.

Westall J., Zachary J. L. and Morel F. M. M. (1976) MINEQL, a computer program for the calculation of chemical equilibrium composition of aqueous systems. *Mass. Inst. Tech. Dept. Civil Eng. Tech. Note* **18**, 91.

Wicks G. G., Lodding A. R. and Molecke M. A. (1993) Aqueous alteration of nuclear waste glasses and metal package components. *MRS Bull.* **XVIII** (9), 32–39.

Witherspoon P.A. and Bodvarsson G.S. (2006) *Geological Challenges in Radioactive Waste Isolation—Fourth Worldwide Review*. LBNL-59808, Lawrence Berkeley National Laboratory and University of California, Berkeley, USA, 295p.

Associate editor: Eric H. Oelkers